Device

Article

Origami self-powered near-sensor computing system using 2D materials for deformation monitoring

Graphical abstract

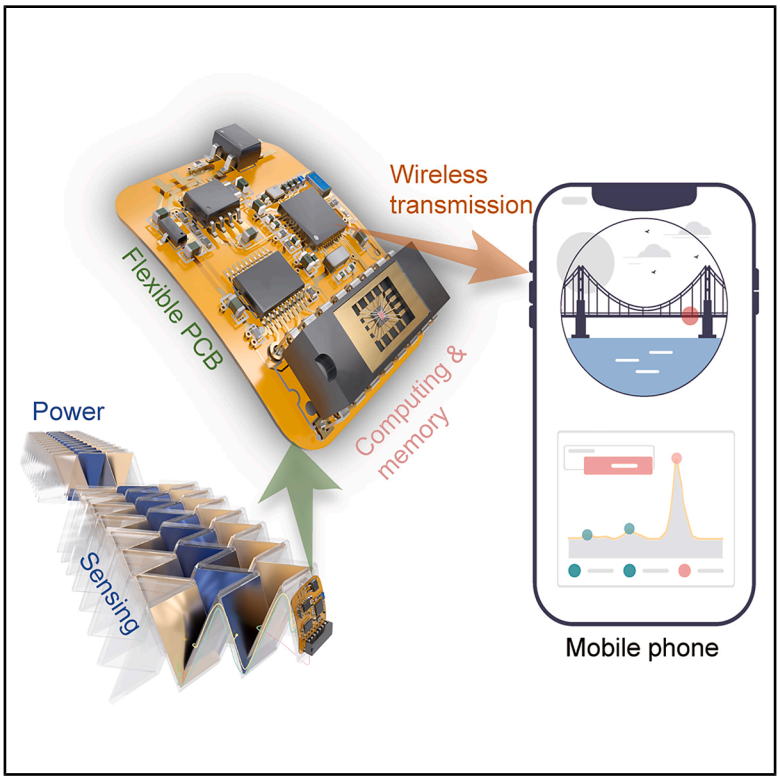

Highlights

- Self-powered deformation near-sensor computing and memory system
- Device integrates an origami-inspired TENG and 2D vermiculite-based RRAM
- Tested for stability over 100,000 cycles and year-level data storage

Authors

Rongjie Zhang (张荣杰), Qinghao Xu (徐庆昊), Yujie Sun (孙宇杰), ..., Wenbo Ding (丁文伯), Hui-Ming Cheng (成会明), Bilu Liu (刘碧录)

Correspondence

ding.wenbo@sz.tsinghua.edu.cn (W.D.), cheng@imr.ac.cn (H.-M.C.), bilu.liu@sz.tsinghua.edu.cn (B.L.)

In brief

Zhang et al. present a self-powered monitoring system that harvests energy from mechanical movements for deformation measurements and computing. Using an origami design and mineral-based memory chips, the device can identify structural changes and transmit the signals in real time.

Zhang et al., 2025, Device *3*, 100933
December 19, 2025 © 2025 Elsevier Inc. All rights are reserved, including those for text and data mining, AI training, and similar technologies.
https://doi.org/10.1016/j.device.2025.100933

CellPress

Device

CellPress

Article

Origami self-powered near-sensor computing system using 2D materials for deformation monitoring

Rongjie Zhang (张荣杰),[1,8] Qinghao Xu (徐庆昊),[2,8] Yujie Sun (孙宇杰),[1] Zenan Lin (林泽南),[2] Keyou Wu (武科佑),[1] Ziwu Song (宋子午),[2] Zhentan Quan (全振潭),[2,3] Huaze Tang (唐华泽),[2] Zihan Wang (王子涵),[2,4] Hongfa Zhao (赵洪发),[2] Shoujie Li (李寿杰),[2] Wenbo Ding (丁文伯),[2,5,*] Hui-Ming Cheng (成会明),[1,6,7,*] and Bilu Liu (刘碧录)[1,9,*]

[1]Shenzhen Geim Graphene Center, Shenzhen Key Laboratory of Advanced Layered Materials for Value-added Applications, Key Laboratory of Electrocatalytic Materials and Green Hydrogen Technology of Guangdong Higher Education Institutes, Institute of Materials Research, Tsinghua Shenzhen International Graduate School, Tsinghua University, Shenzhen 518055, P.R. China

[2]Shenzhen Ubiquitous Data Enabling Key Lab, Institute of Data and Information, Shenzhen International Graduate School, Tsinghua University, Shenzhen 518055, P.R. China

[3]Institute of Materials Research, Center of Double Helix, Shenzhen International Graduate School, Tsinghua University, Shenzhen 518055, P. R. China

[4]Department of Mechanical Engineering, University of California at Berkeley, Berkeley, CA 94720, USA

[5]RISC-V International Open Source Laboratory, Shenzhen 518055, P.R. China

[6]Shenyang National Laboratory for Materials Science, Institute of Metal Research, Chinese Academy of Sciences, Shenyang 110016, P.R. China

[7]Faculty of Materials and Engineering/Institute of Technology for Carbon Neutrality, Shenzhen Institute of Advanced Technology, Chinese Academy of Sciences, Shenzhen 518055, P.R. China

[8]These authors contributed equally

[9]Lead contact

*Correspondence: ding.wenbo@sz.tsinghua.edu.cn (W.D.), cheng@imr.ac.cn (H.-M.C.), bilu.liu@sz.tsinghua.edu.cn (B.L.)

https://doi.org/10.1016/j.device.2025.100933

THE BIGGER PICTURE Real-time structural health monitoring of infrastructure, such as bridges, skyscrapers, and industrial facilities, is crucial for safety and maintenance. Currently, monitoring methods rely on measurements with timed intervals and/or external power sources, which struggle to capture historical deformation or offer life cycle resilience. By integrating a triboelectric nanogenerator with a 2D vermiculite-based memristor in an origami structure, we introduce a self-powered system for deformation sensing, computing, and memory. The system combines an origami-inspired triboelectric device and a matched memristor, offering real-time deformation monitoring with cycle endurance, thermal stability, and year-level durability.

SUMMARY

Structural monitoring is key for buildings and bridges, but existing techniques rely on the integration of multiple systems for sensing, computing, data storage, and power supply. Here, we integrated a triboelectric nanogenerator with a two-dimensional material-based memory, achieving a self-powered capability for deformation monitoring and computing. We adapted an origami-inspired structure to meet the threshold voltage of memory and the two-dimensional vermiculite-based memory. The system exhibits year-level stability, repeatability of over 10^5 cycles, and a response of 60 ns for computing and 24 ms for sensing.

INTRODUCTION

Long-term deformation of building structures can be used to predict structural failure, but traditional methods for obtaining such data can be costly.[1–3] Ideally, historical damage information is captured and stored in real-time over the entire life cycle of the structure.[4] However, existing monitoring techniques face challenges, including delayed response time, high power consumption, and high costs associated with both material and human resources.[5,6]

To address some of these challenges, near-sensor computing systems can offer a viable solution by processing data locally at the sensor interface to minimize transfer latency.[7,8] For instance, analog signals from deformation sensors can be converted into resistive random access memory (RRAM) for resistive switching to achieve near-sensor computing.[9,10] However, this technique still requires a power source. In this regard, a triboelectric nanogenerator (TENG) can be used to provide power by converting mechanical energy into electrical signals.[11–15] One example is the use of a three-terminal transistor couple, with TENG to serve as a gate

All rights are reserved, including those for text and data mining, AI training, and similar technologies.

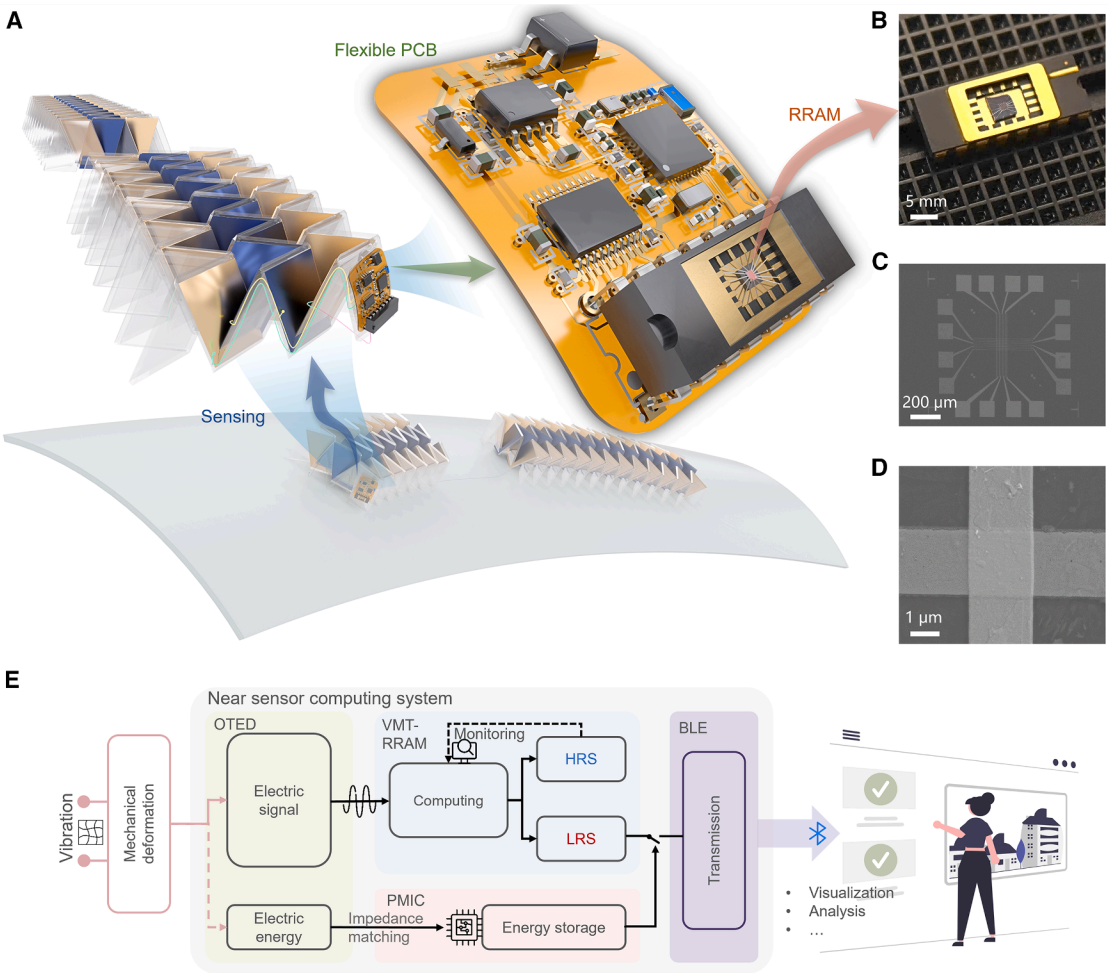

Figure 1. Design of the fully self-powered near-sensor computing system

(A) Schematic of the fully self-powered near-sensor computing system for deformation monitoring. The architecture integrates the following: (1) dual origami-TENG units—one for strain sensing and another dedicated to energy harvesting; (2) VMT-RRAM-based memory-logic modules; and (3) Bluetooth transmission circuitry.

(B–D) (B) Optical photograph and (C and D) scanning electron microscope (SEM) images of the 2D VMT-based RRAM.

(E) Flow chart of the near-sensor computing system. Scale bars: 5 mm in (B), 200 μm in (C), and 1 μm in (D).

terminal within stretchable neuromorphic devices.[16–19] This system achieves self-powered operation and computing logic, but the data storage remains volatile since the data are stored within the transistor channel as different resistance states, and sustaining these computed resistance changes necessitates the continuous application of a source-drain voltage. Consequently, additional power is required to drive the transistor unit. A fully self-powered system could couple the TENG with non-volatile RRAM. However, there exists a mismatch in the switching speed and impedance of RRAM with that of TENG, considering the instantaneous pulse output (with a duration in ms and output in nC) and high internal resistance (GΩ) characteristics of TENG. Two-dimensional (2D) materials have presented the opportunity to operate at nanosecond speeds and with low energy consumption,[20] aligning with the output behaviors of TENG. Nevertheless, RRAMs based on graphene,[21] MoS_2,[22] or h-BN[23] are not suitable for this because of properties such as low off-resistance or compliance current.[24]

Here, we demonstrate an integrated TENG-RRAM system, enabling self-powered and real-time deformation monitoring and computation. The RRAM made of 2D vermiculite (VMT) offers fast switching (60 ns) and high-off impedance (1 GΩ). Meanwhile, the origami-inspired triboelectric device (OTED) is proposed, whose output power can be adjusted flexibly to meet the quantity of deformations. Taking the advantages of the origami structure and matched RRAM, the integrated device shows high cycle endurances (100,000), non-volatile memory (10^4 s), high operating temperature (up to 360 K), and stability (10 weeks).

RESULTS

Operating principle and system design

Figure 1A shows the self-powered near-sensor computing system for structural deformation monitoring. The system consists of two parts, including the sensing part and the computing

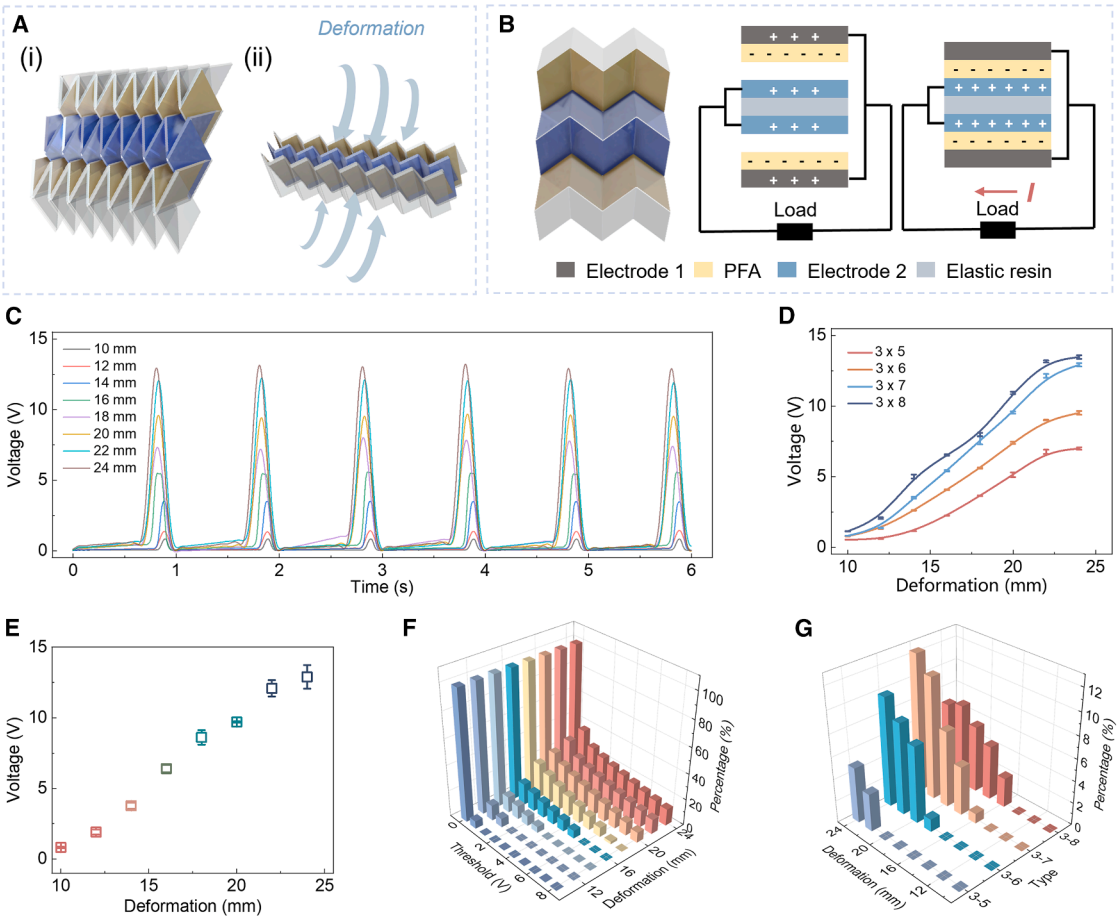

Figure 2. Configuration and characteristics of the OTED

(A) The deformation situation of the OTED. (i) Normal state and (ii) compressed state.

(B) Working mechanism of OTED.

(C) Output curves obtained under different deformation quantities (10–24 mm) using 3 × 7-sized OTED.

(D) Average output performance generated by OTED from various sizes.

(E) Average output performance generated by OTED (3 × 7 size).

(F) The cumulative OTED output time under different threshold values and external excitation conditions.

(G) The percentage of time that exceeds 5.0 V after adding the "mask."

part. The sensing part uses an OTED inspired by the Miura origami structure (Figure S1).[25] Compared to a conventional flat TENG structure, the Miura-folded geometry increases the effective contact area, thereby improving the power output and operational stability (Figure S3).[26] The computation part uses RRAM based on 2D VMT (Figures 1B–1D) with high internal impedance, non-linearity, and rapid switching response that matches the OTED. Consequently, a direct connection between OTED and VMT-RRAM is feasible with minimal deviation from open-circuit voltage to actual output.

We use a flexible printed circuit board (FPCB) to establish the integration of OTED and VMT-RRAM. The designed FPCB is to receive the signal from OTED and establish a connection with the packaged VMT-RRAM chip. The monitoring module will detect the resistance of nodes in the VMT-RRAM chip. When an abnormal node resistance is detected, a wireless signal will be transmitted via Bluetooth low energy (BLE). A capacitor is used to accumulate energy from another TENG for a BLE power supply, as the pulsed output of the TENG cannot directly drive the wireless module. By incorporating an additional energy supply module, we achieved node monitoring and signal transmission every 2 h without the need for external energy input (Figure S2 and Note S4).

Figure 1E provides an overview of the whole system. Initiated by external changes, the induced mechanical deformation generates an analog signal via the OTED. The VMT-RRAM subsequently processes these electrical signals. If the electrical signal remains below the threshold voltage, the system is considered to be in a normal state. If the electrical signals exceed the threshold voltage due to large structural deformation, the VMT-RRAM will transfer from a high-resistance state (HRS) to a non-volatile low-resistance state (LRS). The LRS, which serves as a damage-warning flag, is wirelessly transmitted via BLE.

Characteristics of the OTED

Figure 2A displays the OTED configuration, which follows a predetermined pattern of shape transformations similar to the intricate folds in origami. The geometry of the Miura folding structure improves mechanical-to-electrical energy conversion efficiency compared to a flat TENG (Figure S3). The core substrate uses a 3D-printed flexible resin, in which polyfluoroalkoxy (PFA) and an aluminum (Al) electrode are used as the two contact surfaces for the OTED. The operating mechanism is explained in Figure 2B. When attached to the surface of the monitored object, the OTED converts horizontal axial tensile deformation into a contact/separation state between the PFA and Al on the longitudinal surface. The electron affinity difference between these two materials is notable due to the high fluorine content in PFA and its tendency to lose electrons when in contact with Al. This generates a signal output that stimulates the VMT-RRAM.

The OTED devices of different sizes and arrangements are designed and measured (as 3×5, 3×6, 3×7, and 3×8 arrays; Figure S4). The voltage output of the OTED, exhibits only a 1.2% variation after more than 10,000 cycles of deformations (Figures 2C and S5). The OTED maintains its voltage output within 6% drift after 10^5 high-amplitude (16 mm) cycles (Figure S5B). Furthermore, it exhibits less than 4% variation after 4 months of ambient storage and sustaining operational integrity across extended temperatures from 300 to 360 K, as validated in Figures S5C and S5D. The output voltages of the device reach a value of 12.1 V (from 0.8 to 12.9 V) for a deformation range from 10 to 24 mm (Figure 2D). The voltage output can also be adjusted for suitable sensitivity. For instance, the output of OTED can be adjusted from 2.2 to 6.5 V at deformation of 16 mm (Figure 2E). This tunability can be adjusted through the deformation amplitude and variations in the folding angle, which influence the electrode separation and thereby modulate the electrostatic potential. The OTED's voltage output amplitude remains stable across deformation frequencies from 0.2 to 2.0 Hz (Figure S5F), indicating applicability for monitoring slow structural deformations.

We used the cumulative distribution function[27,28] to analyze the signal output and settle the variability among different devices. This method reduces the impact of short-term fluctuations, enhancing the stability and durability of the voltage output. The analytical approach is derived from its assessment criteria based on the cumulative output time. Figure 2F shows the cumulative OTED output time record under different threshold values and external excitation conditions using the 3×7 size (Figures S6A–S6C for other sizes). Under 16-mm deformation, the proportion of total time with a voltage exceeding the threshold voltage is 6.1% (Figure S6D). The output time can exceed the predefined threshold for an extended duration under certain conditions. Therefore, a masking method is introduced to obtain the optimal device based on the specific output waveform. By evaluating the various conditions, the value of the mask can be determined (Figure S6E and Note S1). For example, given the 16-mm deformation, the calculation results suggest that the 3×7 configuration is the optimal choice (Figure 2G). The discrete output is then transformed into a continuous distribution function, providing a more intuitive display (Figure S6). Based on the Weibull-fitted output distribution, the 3×7 architecture achieves the highest proportion of stable output time above the 5.0 V threshold, only marginally exceeding the threshold, thereby ensuring sensitivity without introducing instability. Consequently, the masking method helps optimize the device configuration for specific application requirements.

Characteristics of the RRAM

The RRAM is fabricated as a passive computing module to connect with the OTED, using the high impedance of 2D VMT. The VMT has a layered structure comprising tetrahedral and octahedral sheets arranged in a 1:2 ratio, and the intra-layers contain exchangeable metallic ions, which provide resistance switching via the migration of ions within VMT.[29] The VMT flakes were produced using a two-step ion exchange strategy,[30] and exhibit monolayer or bilayer distributions with a lateral size of 1–2 μm (Figure S7). Device fabrication employed Langmuir-Blodgett assembly[31] to prepare 10 uniform VMT layers (~15 nm), followed by standard e-beam lithography for electrode patterning (Cr/Au: 10 nm/30 nm, Figures S8 and S9). An 8×8 VMT-RRAM array with a crossbar structure is achieved to demonstrate large-scale device production (Figure 3A).

We measured the electrical behaviors of the VMT-RRAM devices. The devices show a symmetrical and unipolar behavior (Figures S10A–S10C), which can be attributed to transport processes and the migration of internal ions within the VMT inter-layer.[32,33] The operating processes of VMT-RRAM are shown in Figure 3B. The resistive switching originates from voltage-induced formation/rupture of conductive filaments in the VMT layer. Upon the application of an electric field, the internal ions within the VMT nanosheets gradually migrate, causing the formation of conductive filaments and switching of device resistance states. The device can be reset to the initial HRS by applying high voltage, which is due to the electrothermal effect (Note S2). Notice that the different contact electrodes show similar resistive switching characteristics, indicating that the filament formation occurs within the VMT.

Next, the performances of the VMT-RRAM devices are analyzed. Figure 3C presents the time-related switching curves of a device for 100 cycles. The device shows stability during the cycle-to-cycle switching with an on/off ratio range from 10^4 to 10^6, which is suitable for memory.[34,35] Figure 3D shows the statistical average switching voltages for the ON state, which are 5.0 V with a cycle-to-cycle variation (σ/μ) of 10.0%. This allows for direct operation of the devices using OTED with enhanced cycle endurances. The HRS and LRS exhibit different distribution trends in cycle-to-cycle variation (Figure 3E). The LRS distribution ranges from 50 to 500 kΩ, while the HRS distribution ranges from around GΩ to TΩ. This HRS matches the impedance match demands of OTED (exceeding 1 GΩ) (Figure S15A). The calculated reset variation value is 20.0%. The variations in the RRAM reset voltages will not affect the stability of the system because, in the LRS, the output voltage (less than 1 V) of TENG is much lower than the minimum reset voltage of the RRAM.

The device switching speed is a critical factor in matching the short-time pulse output behavior of OTED devices. The device exhibits a fast switching time of 60 ns (Figure 3F), which may be attributed to the tunneling transport processes (Figure S10D and Note S2). The temperature-dependent

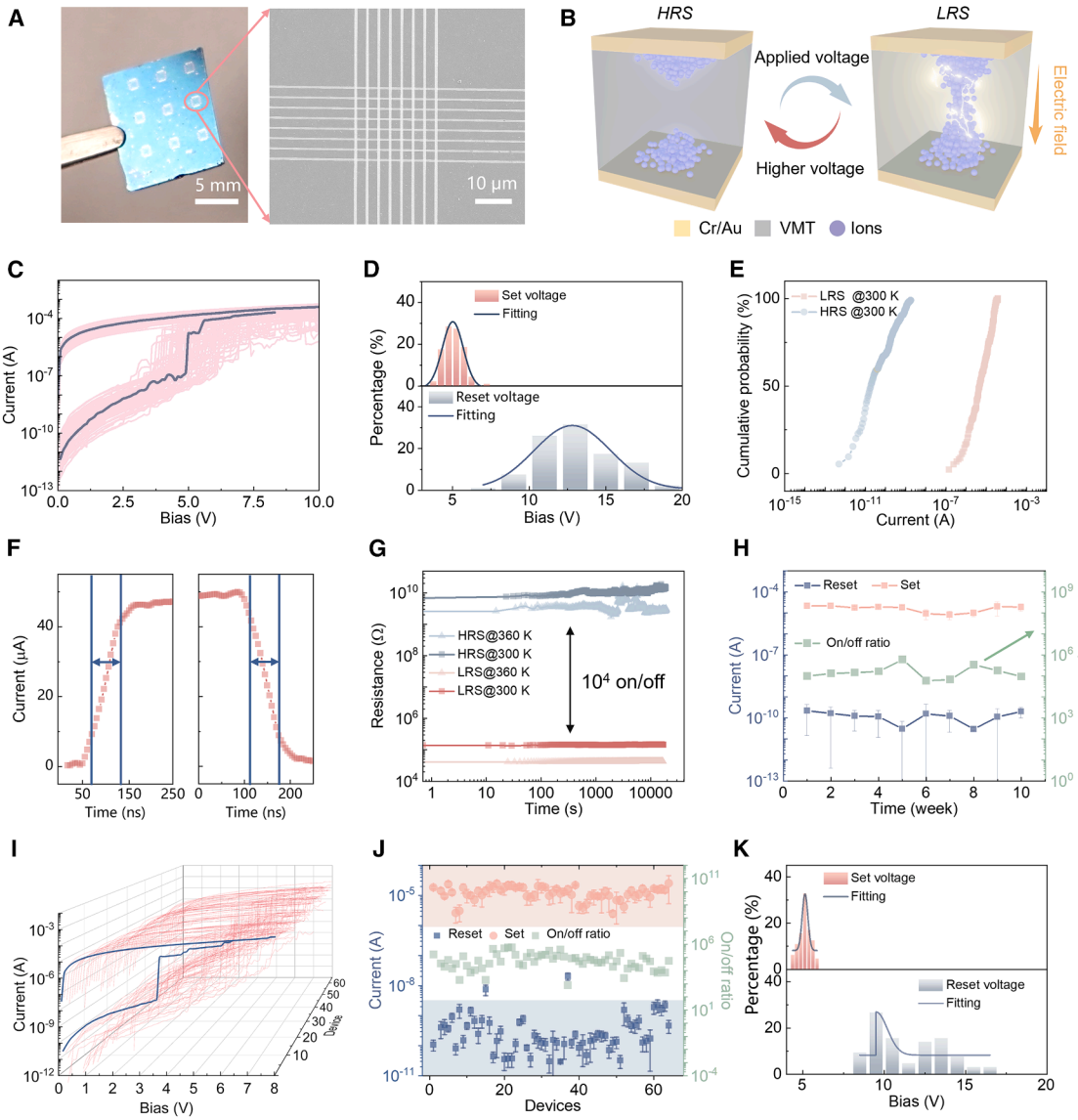

Figure 3. Configuration and characteristics of the 2D VMT RRAMs

(A) The optical microscopy and scanning electron microscopy of the as-fabricated VMT-RRAM arrays.

(B) Operation mechanisms of the VMT-RRAM. The inner ions of VMT re-arrangement under the application of the electrical field contribute to the resistive switching behaviors in VMT-RRAM.

(C) Cycle-to-cycle variations of the VMT-RRAM.

(D) The statistical distribution of set/reset voltages of the VMT-RRAM with different switching cycles.

(E) The statistical distribution of set/reset resistances of the VMT-RRAM with different switching cycles.

(F) The set/reset time of the VMT-RRAM.

(G) Long-term stability of the VMT-RRAM under room temperature and high temperature (360 K).

(H) The set/reset current and on/off ratio of the VMT-RRAM after being exposed to ambient air for ten weeks.

(I–K) (I) The collection *I-V* curves of the 8 × 8 VMT-RRAM array. The statistical distribution of the set/reset current (J) and set/reset voltages (K) of the VMT-RRAM array.

performance of the device is shown in Figure 3G. The long-term stability of both the HRS and LRS is maintained for over 10^4 s (Figure S10F). The device is stable after storing in ambient environments (temperature: 298 ± 5 K, relative humidity: 40–70%) for over 10 weeks due to the chemical inertness of the natural mineral active layer (Figure 3F).

The spatial device-to-device variation is studied by measuring the 8 × 8 device array. We find that all devices display on/off switching responses (Figures S11–S14). The collection of *I-V* curves of the 64 devices is shown in Figure 3I, in which each device is measured 10 times to rule out cycle-to-cycle variations. Statistical uniformity analysis of the 8 × 8 RRAM array confirms

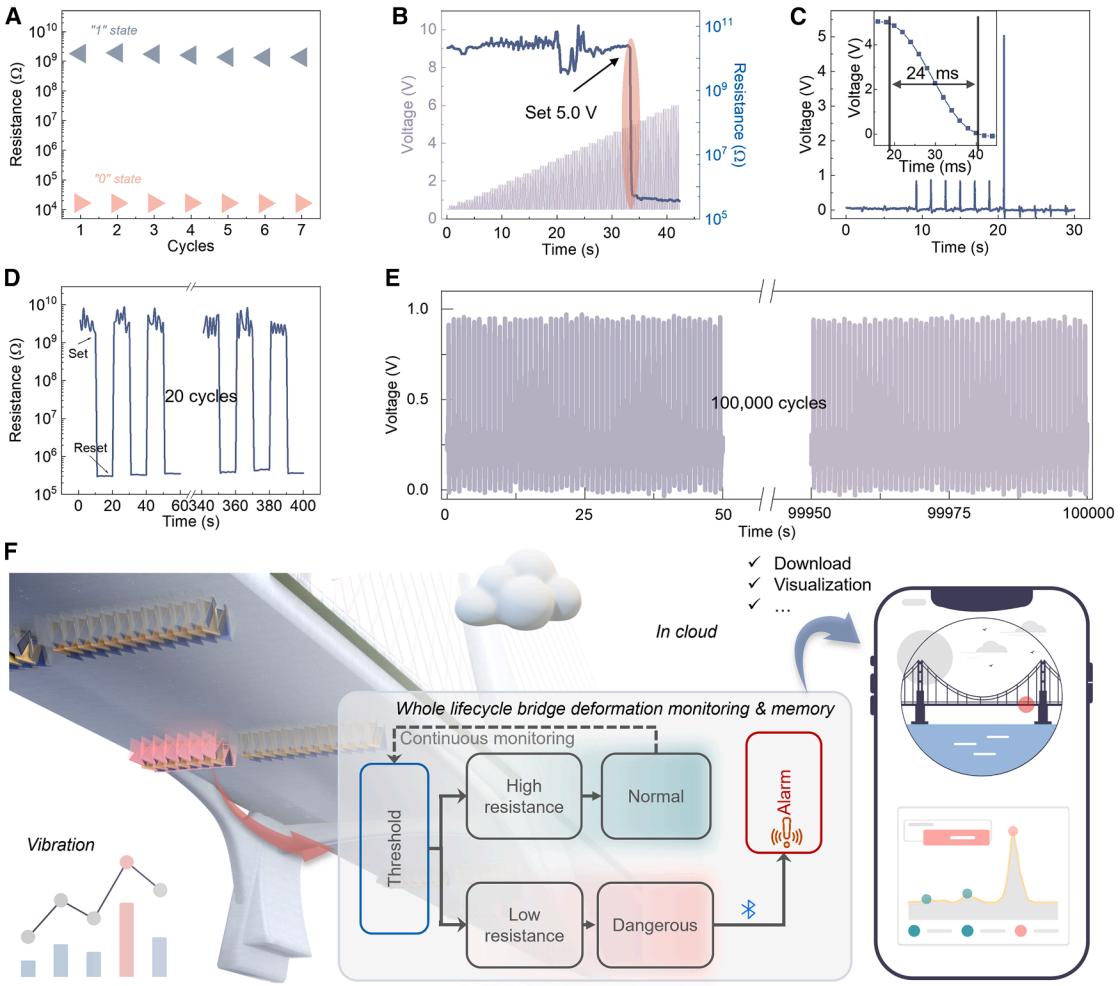

Figure 4. A near-sensor computing system for real-time deformation monitoring

(A) Simulation of the response of VMT-RRAM under two different stimulated voltages by utilizing a semiconductor parameter analyzer.

(B) The response characteristics of VMT-RRAM under continuously increasing voltage.

(C) The output curve of the VMT-RRAM initiated by a large deformation quantity using OTED of 3 × 7 size.

(D) Stability test by experimenting 20 times consecutively.

(E) The output curve of the near-sensor computing system under a small deformation quantity for 100,000 cycles.

(F) Flow chart of the processing for continuous monitoring.

a 100% switching yield. Figure 3J shows the extracted on and off currents of the device under a read voltage of 1.0 V. The intentional ON/OFF ratio tolerance (10^3–10^6) supports binary-state deformation detection via universal threshold (>10^3), while off-state resistance consistency (10^8–10^{11} Ω) ensures TENG power transfer efficiency. The average set and reset voltages are 5.1 V and 13.0 V, respectively (as shown in Figure 3K). These results demonstrate the impedance-matching capability, fast response time, and high stability of a VMT-RRAM to be integrated with the OTED.

Performance demonstration of the integrated VMT-RRAM with OTED

Figure 4 shows the demonstrated self-powered near-sensor computing and memory system. Simulations were conducted to investigate the response of VMT-RRAM under two different stimulated voltages (1.0 and 8.0 V), in accordance with the signal output characteristics of OTED (Figure 4A). The data show a clear and repeatable alteration in resistance values, with VMT-RRAM exhibiting an on/off ratio exceeding 10^5. Next, a continuously increasing voltage is applied to the VMT-RRAM device (from 0.5 to 8.0 V with a voltage increase step of 0.2 V), as shown in Figure 4B. The results demonstrate a substantial change in the resistance state (over 10^4) of the VMT-RRAM after the application of a 5.0 V external stimulation voltage.

The connection of VMT-RRAM to OTED is analyzed. The output of the device remains stable after being connected (Figure S15B). The experiential results are measured when directly integrating the OTED with VMT-RRAM using an OTED with a 3 × 7 size. Slight deformations (<14 mm) applied to the

OTED resulted in a linear increase of voltages in the VMT-RRAM. This is because the generated output voltages applied to the VMT-RRAM have not yet reached the threshold, thereby maintaining a resistance value higher than 1 GΩ (Figure S15C). When the deformation exceeds the predetermined threshold deformation of 16 mm, the OTED generates a large voltage pulse of over 5.0 V. This causes the VMT-RRAM to transit to the LRS, resulting in a decrease in the output voltage applied to the VMT-RRAM. The process is highly responsive, with results obtained within 24 ms (Figure 4C). The system only undergoes one state transition when the deformation extends to 16 mm. By introducing a 20.0-V reset signal through an external circuit, the computing module will revert to its initial state, demonstrating its capacity for repeatable operations. The system maintained a stable operational state after 20 cycles (Figure 4D). The system can maintain a stable operational state when subjected to external deformation (10 mm) over 100,000 cycles (Figures 4E and S14D), enabling long-term stability for deformation monitoring (Note S3 and Figure S16). The entire system operates stably at 360 K (Figures S5D and S10E). Table S1 and Figure S17 compare the operation power and response time of our work against other similar deformation monitoring systems in the existing literature.

Next, we demonstrate an operational software interface designed for the deformation monitor system. The designed fully self-powered near-sensor computing system can effectively meet these needs. The system uses the RRAM to compute and store the large deformations, and the wireless BLE unit converts the signal to a Mobile phone for the user (Figure 4G). As the OTED detects small deformation, it generates an electrical signal that is transmitted directly to the VMT-RRAM, which remains in an HRS. If the building surface undergoes large deformation, the OTED will generate a pulse signal that exceeds a predefined threshold voltage. Consequently, the conductivity of VMT-RRAM changes. The signal is stored and sent by the BLE device as the capacitor accumulates sufficient energy (Figure S17C). Upon receipt of the data at the terminal, it can be disseminated to various user interfaces, enabling portable real-time monitoring. The self-powered system can be achieved by an FPCB design (Videos S1 and S2).

Conclusion and outlook

We develop a system that combines TENG with RRAM to achieve self-powered and real-time deformation monitoring and computing. The origami structure in nanogenerators enables deformation monitoring and stability (over 10^5 cycles). The integrated 2D VMT-RRAMs have a persistent on/off state for 10^4 s and air stability for 10 weeks. We coupled the TENG and RRAM according to the adjustable origami structure and matched the VMT-based memory. The adaptability of this system is demonstrated with wireless remote communication, which shows long-term reliability. This study establishes a foundation system for self-powered deformation monitoring. The humidity and other environmental factors, which have not been tested in this work, can be addressed through encapsulation to ensure application in structural health monitoring. The system's core functionality extends beyond buildings, such as monitoring slope displacement in geotechnical early-warning systems,[36] tracking fatigue deformation on unmanned aerial vehicle wing roots,[37] and assessing rehabilitation when integrated into wearable devices.[38]

METHODS

Materials preparation

The 2D vermiculite (VMT) nanosheets were fabricated by ion exchange processes from bulk VMT powder (Sigma-Aldrich, Figure S9). In brief, the Na^+ and Li^+ ions were used for the complete exchange of inter-layer ions in VMT, and then the ion-exchanged VMT was exfoliated by ultrasonication in the liquid phase. The large-scale VMT thin film was achieved by the Langmuir-Blodgett (LB) assembly process onto a Si/SiO_2 substrate. The VMT-RRAM array was fabricated from five layers of LB assembly VMT thin film.

Device fabrications

Fabrication of the OTED

The fundamental substrate of the OTED was fabricated through 3D printing utilizing the Formlab form3+ in Elastic 50A. After undergoing ethanol-based purification, it was stabilized through the application of ultraviolet light. The sensor's two electrodes were constructed using Cu tape as electrode 1 and Al tape as electrode 2, while the OTED was assembled with polyfluoroalkoxy material serving as the dielectric layer. OTED maintains reliable deformation sensing within −15 to +24 mm, bounded by electrostatic linearity and material failure limits.

Fabrication and encapsulation of the VMT-RRAM array

For the fabrication of the VMT-RRAM device array, the bottom electrodes were defined and fabricated by E-beam lithographic and metal deposition processes and then the VMT thin-film assembly, followed by the fabrication of top electrodes (Figure S8). After contact metal fabrication, the device array was wire-bonded through ultrasonic welding to connect the chip pin. The chip was then placed within a high vacuum environment below 10^{-3} Pa, utilizing a custom metal mold. The chip was gradually heated from room temperature to 340°C at a heating rate of 50 K/s and maintained at this temperature for a duration of 5 min. Subsequently, the temperature was slowly reduced to room temperature at a rate of 30 K/s.

Design and fabrication of the FPCB

The FPCB was designed as an intricate integration of four major segments: a power management circuit, an impedance detection circuit, an OTED signal acquisition circuit, and a BLE communication circuit. The power management circuit employed one of the OTED as the primary energy source. It performs a pivotal function of transforming the AC voltage output of the OTED to DC voltage through the process using full-bridge rectification, subsequently charging the farad capacitor. The impedance detection circuit for an encapsulated chip based on VMT-RRAM was utilized to identify the inherent impedance of the detected nodes. It was powered by the DC power supply and generated varying voltage signals based on the impedance of the detected nodes. These signals were then transmitted to a microcontroller unit for precise voltage recognition. Given the inherent traits of the OTED, namely, a substantial output impedance and a weak signal, the precision operational amplifier

TLC2201 was adopted. TLC2201, with its low power consumption and low input bias current (typical value 1 pA), along with a feedback resistor, feedback capacitor, and the high-precision reference voltage chip TL432, facilitates enhanced monitoring for the output of the OTED. Finally, the BLE communication circuit enables the establishment of a low-power wireless communication channel with the host terminal. It consistently uploads essential data regarding the status of the VMT-RRAM.

Data processing

Sensor outputs were analyzed using Weibull statistical fitting to determine optimal signal distributions and threshold conditions. Briefly, the Weibull distribution parameters (shape k and scale λ) were calculated by maximum likelihood estimation using MATLAB. To ensure device reliability, we employed a masking procedure to filter transient peaks that exceeded the threshold voltage but lacked sufficient stability time. Specifically, signals were retained only if their peak stability fraction exceeded a defined duration threshold, thereby guaranteeing stable operation and data reliability for subsequent RRAM processing.

Measurements

The device structure and morphology were measured by atomic force microscopy (Cypher ES, Oxford Instruments, UK) and scanning electron microscopy (Sigma 300, Carl Zeiss, Germany). Electrical measurements were done with a probe station (Lakeshore, USA), and relevant electrical curves were collected by a semiconductor parameter analyzer (Keithley 6514 and Keithley 4200, USA). The deformation was generated by a programmable linear motor from Linmot. Environmental stability assessments were conducted under controlled ambient conditions: temperature maintained at 298 ± 5 K (room temperature), relative humidity 40%–70%, and atmospheric pressure (101.3 kPa).

RESOURCE AVAILABILITY

Lead contact

Requests for further information and resources should be directed to and will be fulfilled by the lead contact, Bilu Liu (bilu.liu@sz.tsinghua.edu.cn).

Materials availability

This study did not generate new, unique materials.

Data and code availability

Code utilized in this manuscript can be found online.

Any additional data included in this manuscript and the supplemental information are available from the lead contact upon request.

ACKNOWLEDGMENTS

This work was financially supported by the National Science Foundation of China for Distinguished Young Scholars (52125309), the National Key R&D Program (2022YFA1204301), the National Natural Science Foundation of China (52188101, 62104125, 62003188, 62404124, and 52401286), the Natural Science Foundation of Guangdong Province of China (2023A1515011752), the Guangdong Innovative and Entrepreneurial Research Team Program (2021ZT09L197), the Guangdong Basic and Applied Basic Research Foundation (2023A1515110924), the Shenzhen Basic Research Project (JCYJ20220818101014029, JCYJ20230807111619039, JCYJ20220530143013030, and RCBS20231211090548076), the Tsinghua Shenzhen International Graduate School-Shenzhen Pengrui Young Faculty Program of Shenzhen Pengrui Foundation (nos. SZPR2023002 and SZPR2023005), China Postdoctoral Science Foundation (2024M761666), and the Shenzhen Science and Technology Program (ZDSYS20230626091100001).

AUTHOR CONTRIBUTIONS

R.Z. and Q.X. conceived the idea and methodology, developed the whole life cycle deformation monitoring system, and wrote the manuscript. K.W. prepared the vermiculite thin film. Z.L. measured the properties of TENG. Y.S. measured the electrical properties of the RRAM. Z.S. and Z.Q. fabricated the TENG device. H.T. and Z.W. assisted in developing the origami structure. H.Z. and S.L. helped with the circuit system. W.D., B.L., and H.-M.C. supervised this work.

DECLARATION OF INTERESTS

There are no conflicts of interest to declare.

SUPPLEMENTAL INFORMATION

Supplemental information can be found online at https://doi.org/10.1016/j.device.2025.100933.

Received: June 2, 2025
Revised: June 16, 2025
Accepted: August 26, 2025
Published: September 17, 2025

REFERENCES

1. Zeng, Q., Tian, X., Nguyen, D.T., Li, C., Chia, P., Tee, B.C.K., Wu, C., and Ho, J.S. (2024). A digitally embroidered metamaterial biosensor for kinetic environments. Nat. Electron. *7*, 1025–1034. https://doi.org/10.1038/s41928-024-01263-4.
2. Nguyen, D.T., Zeng, Q., Tian, X., Chia, P., Wu, C., Liu, Y., and Ho, J.S. (2024). Ambient health sensing on passive surfaces using metamaterials. Sci. Adv. *10*, eadj6613. https://doi.org/10.1126/sciadv.adj6613.
3. Favarelli, E., and Giorgetti, A. (2021). Machine learning for automatic processing of modal analysis in damage detection of bridges. IEEE Trans. Instrum. Meas. *70*, 1–13. https://doi.org/10.1109/TIM.2020.3038288.
4. Zhong, Y., Tang, J., Li, X., Liang, X., Liu, Z., Li, Y., Xi, Y., Yao, P., Hao, Z., Gao, B., et al. (2022). A RRAM-based analogue reservoir computing system for real-time and power-efficient signal processing. Nat. Electron. *5*, 672–681. https://doi.org/10.1038/s41928-022-00838-3.
5. Kim, J., Campbell, A.S., de Ávila, B.E.F., and Wang, J. (2019). Wearable biosensors for healthcare monitoring. Nat. Biotechnol. *37*, 389–406. https://doi.org/10.1038/s41587-019-0045-y.
6. Wang, T., Meng, J., Zhou, X., Liu, Y., He, Z., Han, Q., Li, Q., Yu, J., Li, Z., Liu, Y., et al. (2022). Reconfigurable neuromorphic RRAM network for ultralow-power smart textile electronics. Nat. Commun. *13*, 7432. https://doi.org/10.1038/s41467-022-35160-1.
7. Zhou, F., and Chai, Y. (2020). Near-sensor and in-sensor computing. Nat. Electron. *3*, 664–671. https://doi.org/10.1038/s41928-020-00501-9.
8. Yang, Y. (2019). Multi-tier computing networks for intelligent IoT. Nat. Electron. *2*, 4–5. https://doi.org/10.1038/s41928-018-0195-9.
9. Zhang, X., Zhuo, Y., Luo, Q., Wu, Z., Midya, R., Wang, Z., Song, W., Wang, R., Upadhyay, N.K., Fang, Y., et al. (2020). An artificial spiking afferent nerve based on Mott RRAMs for neurorobotics. Nat. Commun. *11*, 51. https://doi.org/10.1038/s41467-019-13827-6.
10. Wang, M., Tu, J., Huang, Z., Wang, T., Liu, Z., Zhang, F., Li, W., He, K., Pan, L., Zhang, X., et al. (2022). Tactile near-sensor analogue computing for ultrafast responsive artificial skin. Adv. Mater. *34*, 2201962. https://doi.org/10.1002/adma.202201962.

11. Fan, F.R., Tian, Z.Q., and Lin Wang, Z. (2012). Flexible triboelectric generator. Nano Energy *1*, 328–334. https://doi.org/10.1016/j.nanoen.2012.01.004.

12. Jin, T., Sun, Z., Li, L., Zhang, Q., Zhu, M., Zhang, Z., Yuan, G., Chen, T., Tian, Y., Hou, X., and Lee, C. (2020). Triboelectric nanogenerator sensors for soft robotics aiming at digital twin applications. Nat. Commun. *11*, 5381. https://doi.org/10.1038/s41467-020-19059-3.

13. Wang, T., Wang, C., Zeng, Q., Gu, G., Wang, X., Cheng, G., and Du, Z. (2024). A real-time, self-powered wireless pressure sensing system with efficient coupling energy harvester, sensing, and communication modules. Nano Energy *125*, 109533. https://doi.org/10.1016/j.nanoen.2024.109533.

14. Zhang, W., Gu, G., Ren, H., Zhang, Z., Zhang, Z., Qin, H., Zheng, M., Du, Z., and Cheng, G. (2025). A real-time self-powered wireless pressure sensing system based on capacitive triboelectric pressure sensor. Nano Energy *136*, 110729. https://doi.org/10.1016/j.nanoen.2025.110729.

15. Yu, J., Gao, G., Huang, J., Yang, X., Han, J., Zhang, H., Chen, Y., Zhao, C., Sun, Q., and Wang, Z.L. (2021). Contact-electrification-activated artificial afferents at femtojoule energy. Nat. Commun. *12*, 1581. https://doi.org/10.1038/s41467-021-21890-1.

16. Dai, S., Dai, Y., Zhao, Z., Xia, F., Li, Y., Liu, Y., Cheng, P., Strzalka, J., Li, S., Li, N., et al. (2022). Intrinsically stretchable neuromorphic devices for on-body processing of health data with artificial intelligence. Matter *5*, 3375–3390. https://doi.org/10.1016/j.matt.2022.07.016.

17. Liu, Y., Liu, D., Gao, C., Zhang, X., Yu, R., Wang, X., Li, E., Hu, Y., Guo, T., and Chen, H. (2022). Self-powered high-sensitivity all-in-one vertical tribotransistor device for multi-sensing-memory-computing. Nat. Commun. *13*, 7917. https://doi.org/10.1038/s41467-022-35628-0.

18. Cheng, J., Ding, W., Zi, Y., Lu, Y., Ji, L., Liu, F., Wu, C., and Wang, Z.L. (2018). Triboelectric microplasma powered by mechanical stimuli. Nat. Commun. *9*, 3733. https://doi.org/10.1038/s41467-018-06198-x.

19. Zhang, C., He, L., Zhou, L., Yang, O., Yuan, W., Wei, X., Liu, Y., Lu, L., Wang, J., and Wang, Z.L. (2021). Active resonance triboelectric nanogenerator for harvesting omnidirectional water-wave energy. Joule *5*, 1613–1623. https://doi.org/10.1016/j.joule.2021.04.016.

20. Xu, R., Jang, H., Lee, M.-H., Amanov, D., Cho, Y., Kim, H., Park, S., Shin, H.-J., and Ham, D. (2019). Vertical MoS_2 double-layer RRAM with electrochemical metallization as an atomic-scale synapse with switching thresholds approaching 100 mV. Nano Lett. *19*, 2411–2417. https://doi.org/10.1021/acs.nanolett.8b05140.

21. Schranghamer, T.F., Oberoi, A., and Das, S. (2020). Graphene memristive synapses for high precision neuromorphic computing. Nat. Commun. *11*, 5474. https://doi.org/10.1038/s41467-020-19203-z.

22. Wang, M., Cai, S., Pan, C., Wang, C., Lian, X., Zhuo, Y., Xu, K., Cao, T., Pan, X., Wang, B., et al. (2018). Robust RRAMs based on layered two-dimensional materials. Nat. Electron. *1*, 130–136. https://doi.org/10.1038/s41928-018-0021-4.

23. Chen, S., Mahmoodi, M.R., Shi, Y., Mahata, C., Yuan, B., Liang, X., Wen, C., Hui, F., Akinwande, D., Strukov, D.B., et al. (2020). Wafer-scale integration of two-dimensional materials in high-density memristive crossbar arrays for artificial neural networks. Nat. Electron. *3*, 638–645. https://doi.org/10.1038/s41928-020-00473-w.

24. Hus, S.M., Ge, R., Chen, P.-A., Liang, L., Donnelly, G.E., Ko, W., Huang, F., Chiang, M.-H., Li, A.-P., and Akinwande, D. (2021). Observation of single-defect RRAM in an MoS_2 atomic sheet. Nat. Nanotechnol. *16*, 58–62. https://doi.org/10.1038/s41565-020-00789-w.

25. Schenk, M., and Guest, S.D. (2013). Geometry of Miura-folded metamaterials. Proc. Natl. Acad. Sci. USA *110*, 3276–3281. https://doi.org/10.1007/s12274-021-3401-4.

26. Li, G., Liu, G., He, W., Long, L., Li, B., Wang, Z., Tang, Q., Liu, W., and Hu, C. (2021). Miura folding based charge-excitation triboelectric nanogenerator for portable power supply. Nano Res. *14*, 4204–4210.

27. Alavi, A.H., Hasni, H., Lajnef, N., and Chatti, K. (2016). Damage growth detection in steel plates: Numerical and experimental studies. Eng. Struct. *128*, 124–138. https://doi.org/10.1016/j.engstruct.2016.09.026.

28. Hasni, H., Alavi, A.H., Lajnef, N., Abdelbarr, M., Masri, S.F., and Chakrabartty, S. (2017). Self-powered piezo-floating-gate sensors for health monitoring of steel plates. Eng. Struct. *148*, 584–601. https://doi.org/10.1016/j.engstruct.2017.06.063.

29. Zhang, R., Chen, W., Teng, C., Liao, W., Liu, B., and Cheng, H.M. (2021). Realization of a non-Markov chain in a single 2D mineral RRAM. Sci. Bull. *66*, 1634–1640. https://doi.org/10.1016/j.scib.2021.04.025.

30. Huang, Z., Lan, T., Dai, L., Zhao, X., Wang, Z., Zhang, Z., Li, B., Li, J., Liu, J., Ding, B., et al. (2022). 2D Functional minerals as sustainable materials for magneto-optics. Adv. Mater. *34*, 2110464. https://doi.org/10.1002/adma.202110464.

31. Wang, J., Teng, C., Zhang, Z., Chen, W., Tan, J., Pan, Y., Zhang, R., Zhou, H., Ding, B., Cheng, H.M., and Liu, B. (2021). A Scalable Artificial Neuron Based on Ultrathin Two-Dimensional Titanium Oxide. ACS Nano *15*, 15123–15131. https://doi.org/10.1021/acsnano.1c05565.

32. Larentis, S., Nardi, F., Balatti, S., Gilmer, D.C., and Ielmini, D. (2012). Resistive switching by voltage-driven ion migration in bipolar RRAM—Part II: Modelinsg. IEEE Trans. Electron. Dev. *59*, 2468–2475. https://doi.org/10.1109/TED.2012.2202320.

33. Tian, H., Wang, X.-F., Mohammad, M.A., Gou, G.-Y., Wu, F., Yang, Y., and Ren, T.-L. (2018). A hardware Markov chain algorithm realized in a single device for machine learning. Nat. Commun. *9*, 4305. https://doi.org/10.1038/s41467-018-06644-w.

34. Tang, B., Veluri, H., Li, Y., Yu, Z.G., Waqar, M., Leong, J.F., Sivan, M., Zamburg, E., Zhang, Y.-W., Wang, J., and Thean, A.V.Y. (2022). Wafer-scale solution-processed 2D material analog resistive memory array for memory-based computing. Nat. Commun. *13*, 3037. https://doi.org/10.1038/s41467-022-30519-w.

35. Zhang, R., Lai, Y., Chen, W., Teng, C., Sun, Y., Yang, L., Wang, J., Liu, B., and Cheng, H.M. (2022). Carrier trapping in wrinkled 2D monolayer MoS_2 for ultrathin memory. ACS Nano *16*, 6309–6316. https://doi.org/10.1021/acsnano.2c00350.

36. Macciotta, R., Hendry, M., and Martin, C.D. (2016). Developing an early warning system for a very slow landslide based on displacement monitoring. Nat. Hazards *81*, 887–907. https://doi.org/10.1007/s11069-015-2110-2.

37. Xu, Z., Cao, L.N.Y., Li, C., Luo, Y., Su, E., Wang, W., Tang, W., Yao, Z., and Wang, Z.L. (2023). Digital mapping of surface turbulence status and aerodynamic stall on wings of a flying aircraft. Nat. Commun. *14*, 2792. https://doi.org/10.1038/s41467-023-38486-6.

38. Wang, Y., Gao, Z., Wu, W., Xiong, Y., Luo, J., Sun, Q., Mao, Y., and Wang, Z.L. (2025). TENG-Boosted Smart Sports with Energy Autonomy and Digital Intelligence. Nano-Micro Lett. *17*, 265. https://doi.org/10.1007/s40820-025-01778-1.